

An efficient 3D non-hydrostatic model for simulating near-shore breaking waves



Jingxin Zhang^{a,b,*}, Dongfang Liang^{a,b}, Hua Liu^{a,b}

^a MOEKey Laboratory of Hydrodynamics, Shanghai Jiao Tong University, Shanghai 200240, China

^b School of Naval Architecture, Ocean and Civil Engineering, Shanghai Jiao Tong University, Shanghai 200240, China

ARTICLE INFO

Keywords:

Non-hydrostatic pressure distribution

Wave breaking

TVD

Wave dispersion

Shock waves

ABSTRACT

This paper describes the formulation and verification of a 3D non-hydrostatic free surface water flow model with a Finite Volume Method (FVM) on unstructured grids. The model extends the Non-linear Shallow Water (NSW) equations by utilizing a non-hydrostatic pressure term for describing dispersive water waves. In order to simulate the near-shore wave dynamics, the wave breaking is modeled using a so-called splitting algorithm in the present model. When a wave is ready to break, the non-hydrostatic model is locally switched to the hydrostatic model to suppress the dispersive effects. The breaking wave front is analogy to a moving hydraulic jump, and is treated as a shock with its energy dissipation implicitly evaluated according to the shock-wave theory. The wave breaking is then simulated by solving the conventional NSW with a 2nd order Total Variation Diminishing (TVD) scheme. Extensive case studies are carried out to verify the efficiency and accuracy of the model. The numerical simulations are found to agree well with the experimental measurements.

1. Introduction

Many flows in natural environments are confined between a solid bed beneath and a free surface above the water body. These flows are common in oceanic shelves, estuaries, and rivers, and they are generally referred to as shallow water flows (Borthwick and Barber, 1992; Fringer et al., 2006; Liang et al., 2006; Zhang and Liu, 2009). Such flows are traditionally described by the Non-linear Shallow Water equations (NSW). Researchers have made significant progress to solve this kind of models. The efficient solutions of the NSW enable the modeling of large-scale long wave dynamics, such as tides, storm surges, and tsunamis. Despite the advancements, the difficulties in connection with breaking and dispersive waves in the near-shore region remain unresolved.

To improve the handling of dispersive water waves, the NSW has been developed to account for the non-hydrostatic pressure distribution. Casulli (1999) and Casulli and Zanolli (2002) reported a fully-hydrodynamic pressure treatment that expresses the pressure as a sum of the hydrostatic and non-hydrostatic constituents. Jankowski (1999) presented the details of a predictor-corrector method for the calculation of the pressure field. Such a non-hydrostatic model has been widely implemented in the Cartesian coordinate system (Li and Fleming, 2001; Kocyigit et al., 2002; Chen, 2003) and the unstructured grid system (Fringer et al., 2006). The models of this kind have been

used to simulate dispersive waves and flows in the domains with complex geometries (Zhang et al., 2014).

The non-hydrostatic model enables the expansion of the application of the NSW from long waves to relatively short waves, i.e. from non-dispersive waves to dispersive waves. However, few applications to the near-shore region have been carried out by this kind of models because of their inability to handle wave breaking. To model wave breaking, the Navier-Stokes equations with Volume of Fluid (VOF) treatment is able to simulate the complex free surface transformation and breakage, but the high computational costs restrict their practical applications involving natural coasts. Besides of the VOF method for capturing the free surface, the Smoothed Particle Hydrodynamics (SPH) model is a powerful, but computationally-demanding, mesh-free technique for simulating free surface flows, with violent breaking waves (Liang, 2010; Pu et al., 2013; Chen et al., 2015). Compared with the highly accurate numerical models capable of representing the full spectrum of wave dynamics, the Non-linear Shallow Water equations (NSW) and Boussinesq-type (BT) models are still more widely used for simulating the near-shore wave dynamics because of their lower computational costs. However, the NSW cannot represent wave dispersion and the BT models cannot handle wave breaking. The earlier methods of modeling the wave breaking with the BT models are by means of introducing an extra wave energy dissipation term in the governing equations (Zelt, 1991; Karambas and Koutitas, 1992; Schäffer et al., 1993; Kennedy

* Corresponding author at: School of Naval Architecture, Ocean and Civil Engineering, Shanghai Jiao Tong University, China.
E-mail address: zhangjingxin@sjtu.edu.cn (J. Zhang).

et al., 2000; Cienfuegos et al., 2010). Recently, a family of fully-nonlinear BT model were proposed for simulating wave breaking with a splitting algorithm (Bonneton et al., 2011b; Tissier et al., 2012). The idea is to switch the numerical model from the BT equations to the NSW equations when the waves are about to break. In this way, the non-physical dispersive behavior of waves at steep water surface gradients is avoided and the mechanical energy dissipation associated with the wave breaking is modeled by the shock theory. Similar ideas have been adopted in non-hydrostatic models. Ma et al. (2012) described a NHWAVE non-hydrostatic numerical model for simulating the wave dynamics in the surf and swash zones, based on a type of combined FVM and FDM on structured grids. The NHWAVE model is extended to simulate breaking waves using shock-capturing schemes. The similar numerical method was also adopted by Pieter et al. (2013, 2014) in a vertical 2D non-hydrostatic model for investigating coastal processes, and by Wei and Jia (2014) in a non-hydrostatic finite element model for studying coastal waves. Coupled with an efficient numerical technique to handle wave breaking, the non-hydrostatic models are expected to be supervisor to the depth-integrated models in modeling coastal wave dynamics.

In this paper, an in-house code named HydroFlow® was developed, which is a 3D non-hydrostatic FVM model on unstructured grids. Similar to the splitting algorithm used in the BT model, the non-hydrostatic equations are replayed by the hydrostatic equations at the local wave front when wave breaking occurs. Several case studies with available experimental data are used to validate the present model's performance in predicting wave transformation, breaking and run-up on beaches.

2. Numerical model

2.1. Governing equations

The non-hydrostatic pressure distribution is implemented in the model by representing the total pressure as a superposition of the hydrostatic component p_h and the non-hydrostatic p_n component (Casulli, 1999). In order to accurately capture the shapes of the free surface and the uneven bottom boundary, the vertical coordinate z is transformed to the σ coordinate, and the transformed equations can be rewritten as:

$$\frac{\partial \zeta}{\partial t} + \frac{\partial q_x}{\partial x} + \frac{\partial q_y}{\partial y} + \frac{\partial q_\sigma}{\partial \sigma} = 0 \quad (1)$$

$$\begin{aligned} \frac{\partial q_x}{\partial t} + \frac{\partial q_x u}{\partial x} + \frac{\partial q_x v}{\partial y} + \frac{\partial q_x \tilde{w}}{\partial \sigma} = & -gD \frac{\partial \zeta}{\partial x} - \frac{D}{\rho_0} \frac{\partial p_n}{\partial x} + f q_y + \frac{\partial}{\partial x} \left(v_t \frac{\partial q_x}{\partial x} \right) \\ & + \frac{\partial}{\partial y} \left(v_t \frac{\partial q_x}{\partial y} \right) + \frac{1}{D} \frac{\partial}{\partial \sigma} \left(\frac{v_t}{D} \frac{\partial q_x}{\partial \sigma} \right) \end{aligned} \quad (2)$$

$$\begin{aligned} \frac{\partial q_y}{\partial t} + \frac{\partial q_y u}{\partial x} + \frac{\partial q_y v}{\partial y} + \frac{\partial q_y \tilde{w}}{\partial \sigma} = & -gD \frac{\partial \zeta}{\partial y} - \frac{D}{\rho_0} \frac{\partial p_n}{\partial y} - f q_x + \frac{\partial}{\partial x} \left(v_t \frac{\partial q_y}{\partial x} \right) \\ & + \frac{\partial}{\partial y} \left(v_t \frac{\partial q_y}{\partial y} \right) + \frac{1}{D} \frac{\partial}{\partial \sigma} \left(\frac{v_t}{D} \frac{\partial q_y}{\partial \sigma} \right) \end{aligned} \quad (3)$$

$$\begin{aligned} \frac{\partial q_z}{\partial t} + \frac{\partial q_z u}{\partial x} + \frac{\partial q_z v}{\partial y} + \frac{\partial q_z \tilde{w}}{\partial \sigma} = & -\frac{1}{\rho_0} \frac{\partial p_n}{\partial \sigma} + \frac{\partial}{\partial x} \left(v_t \frac{\partial q_z}{\partial x} \right) + \frac{\partial}{\partial y} \left(v_t \frac{\partial q_z}{\partial y} \right) \\ & + \frac{1}{D} \frac{\partial}{\partial \sigma} \left(\frac{v_t}{D} \frac{\partial q_z}{\partial \sigma} \right) \end{aligned} \quad (4)$$

where $q_x = Du$, $q_y = Dv$, $q_z = Dw$, $q_\sigma = D\tilde{w}$, u , v , w are the velocities in x , y , z directions, respectively, and the velocity along the σ coordinate is calculated as:

$$q_\sigma = \frac{q_z}{D} - \frac{q_x}{D} \left(\sigma \frac{\partial D}{\partial x} + \frac{\partial \zeta}{\partial x} \right) - \frac{q_y}{D} \left(\sigma \frac{\partial D}{\partial y} + \frac{\partial \zeta}{\partial y} \right) - \left(\sigma \frac{\partial D}{\partial t} + \frac{\partial \zeta}{\partial t} \right) \quad (5)$$

In the above equations, g is gravitational acceleration, $f = 2\omega \sin \phi$ is the Coriolis force coefficient, ϕ is the latitude, ω is the Earth's angular speed, ζ is the free surface elevation, h is the still water depth, and $D = h + \zeta$ is the total water depth. When the non-hydrostatic pressure p_n is ignored, then the vertical momentum equation should be also neglected. Then, the system described by Eqs. (1)–(4) degenerates to the conventional shallow water model that consists of only the horizontal momentum equations and the continuity equation.

2.2. Turbulence model

To close the system, the eddy viscosity concept is adopted in the present study and the eddy viscosity coefficient ν_t is determined using the one-equation Spalart-Allmaras (SA) model (Spalart et al., 2000). The transport equation for $\tilde{\nu}$ is:

$$\frac{D\tilde{\nu}}{Dt} = c_{b1}\tilde{S}\tilde{\nu} - c_{w1}f_w \left(\frac{\tilde{\nu}}{d} \right)^2 + \frac{1}{\sigma} \{ \nabla \cdot [(\nu + \tilde{\nu}) \nabla \tilde{\nu}] + c_{b2}(\nabla \tilde{\nu})^2 \} \quad (6)$$

where

$$\begin{aligned} \chi & \equiv \frac{\tilde{\nu}}{\nu}, f_w = g_1 \left[\frac{1 + c_{w3}}{g^6 + c_{w3}} \right]^{1/6}, g_1 = r + c_{w2}(r^6 - r), r \equiv \frac{\tilde{\nu}}{\tilde{S}\kappa^2 d^2}, \tilde{S} \\ & = |\tilde{S}| + \frac{\tilde{\nu}}{\kappa^2 d^2} f_{v2}, f_{v1} = \frac{\chi^3}{\chi^3 + c_{v1}^3}, f_{v2} = 1 - \frac{\chi}{1 + \chi f_{v1}}, \tilde{S}_{ij} \\ & = \frac{1}{2} \left(\frac{\partial \tilde{u}_i}{\partial x_j} + \frac{\partial \tilde{u}_j}{\partial x_i} \right), \end{aligned}$$

and d is the distance to the nearest solid wall. The model constants are:

$$\begin{aligned} c_{b1} &= 0.1355, \sigma = 2/3, c_{b2} = 0.622, \kappa = 0.41, c_{w1} \\ &= c_{b1}/\kappa^2 + (1 + c_{b2})/\sigma, c_{w2} = 0.3, c_{w3} = 2.0, c_{v1} = 7.1 \end{aligned}$$

The eddy viscosity ν_t is then computed according to:

$$\nu_t = \tilde{\nu} f_{v1} \quad (7)$$

2.3. Numerical scheme

The numerical model is based on the multi-layered discretization on unstructured grids and the σ -coordinate transformation in the vertical direction, as shown in Fig. 1. On the cell faces, a non-orthogonal horizontal local coordinate system (ξ , η) is used to replace the global Cartesian coordinates (x , y). The derivatives of a function ϕ on the cell face are carried out in the local coordinates, which are presented as:

$$\phi_x = \frac{1}{J} (\phi_\xi y_\eta - \phi_\eta y_\xi), \quad \phi_y = \frac{1}{J} (\phi_\eta x_\xi - \phi_\xi x_\eta), \quad J = x_\xi y_\eta - x_\eta y_\xi \quad (8)$$

where ξ is directed from a Control Cell (CC) center to a Neighboring Cell (NC) center across the common face, and η is directed along the common boundary and in the anticlockwise direction around the ξ

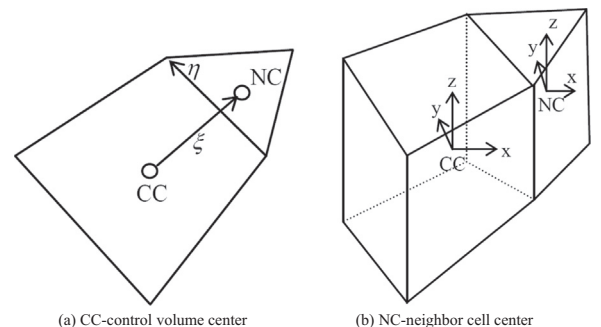


Fig. 1. Local coordinates of the control volume. (a) CC-control volume center (b) NC-neighbor cell center.

coordinate, as shown in Fig. 1.

The finite volume formulation of the governing equations uses a series of 2nd order TVD discretization. The fast-propagating gravity waves are numerically solved by a semi-implicit scheme proposed by Casulli and Cattani (1994) to improve the numerical stability. As all the flow variables are stored at the cell centers, an arbitrary variable $\langle \varphi \rangle^f$ at the cell face can be calculated to be:

$$\langle \varphi \rangle^f = \varphi_c + \frac{1}{2} \psi(r_f)(\varphi_D - \varphi_C) \quad (9)$$

where f denotes the cell face, φ_D and φ_C are, respectively, the cell-centered variants in the downwind and upwind nodes of the face f . Using a flux limiter $\psi(r_f)$, one can obtain a high order TVD scheme. The ratio r_f is calculated using the method proposed by (Darwish and Moukalled, 2003):

$$r_f = \frac{2 \nabla \varphi_c \cdot \vec{e}_D}{\varphi_D - \varphi_C} - 1 \quad (10)$$

In this paper, the OSHER limiter $\psi(r_f) = \max(0, \min(2, r_f))$ is adopted for all the case studies.

The total hydrodynamic pressure is decomposed into the hydrostatic and non-hydrostatic parts, so a splitting strategy is needed, which is named as the predictor-corrector scheme (Jankowski, 1999). In the predictor step, only the hydrostatic pressure is considered, while the non-hydrostatic pressure is solved in the following corrector step.

The continuity equation is discretized as:

$$\begin{aligned} \frac{\zeta_i^{n+1} - \zeta_i^n}{\Delta t} + \theta \sum_{k=1}^{KBM} \left(\frac{\partial q_{x,k}^{n+1}}{\partial x} \right)_{i,k} \Delta \sigma_k + (1 - \theta) \sum_{k=1}^{KBM} \left(\frac{\partial q_x^n}{\partial x} \right)_{i,k} \Delta \sigma_k \\ + \theta \sum_{k=1}^{KBM} \left(\frac{\partial q_{y,k}^{n+1}}{\partial y} \right)_{i,k} \Delta \sigma_k + (1 - \theta) \sum_{k=1}^{KBM} \left(\frac{\partial q_y^n}{\partial y} \right)_{i,k} \Delta \sigma_k = 0 \end{aligned} \quad (11)$$

where KBM is the number of layers in the vertical direction, and Δt is the time integration step. The discretized momentum equations are written as:

$$\begin{aligned} \frac{q_{xi,k}^{n+1} - q_{xi,k}^n}{\Delta t} = F q_{xi,k}^n - g D \theta \left(\frac{\partial \zeta^{n+1}}{\partial x} \right)_{i,k} - g D (1 - \theta) \left(\frac{\partial \zeta^n}{\partial x} \right)_{i,k} \\ - \frac{D}{\rho_0} \left(\frac{\partial p_n^{n+1}}{\partial x} \right)_{i,k} + \left[\frac{\partial}{\partial \sigma} \left(\frac{\nu_t}{D} \frac{\partial q_x^{n+1}}{\partial \sigma} \right) \right]_{i,k} \end{aligned} \quad (12)$$

$$\begin{aligned} \frac{q_{yi,k}^{n+1} - q_{yi,k}^n}{\Delta t} = F q_{yi,k}^n - g D \theta \left(\frac{\partial \zeta^{n+1}}{\partial y} \right)_{i,k} - g D (1 - \theta) \left(\frac{\partial \zeta^n}{\partial y} \right)_{i,k} \\ - \frac{D}{\rho_0} \left(\frac{\partial p_n^{n+1}}{\partial y} \right)_{i,k} + \left[\frac{\partial}{\partial \sigma} \left(\frac{\nu_t}{D} \frac{\partial q_y^{n+1}}{\partial \sigma} \right) \right]_{i,k} \end{aligned} \quad (13)$$

$$\frac{q_{zi,k}^{n+1} - q_{zi,k}^n}{\Delta t} = F q_{zi,k}^n - \frac{1}{\rho_0} \left(\frac{\partial p_n^{n+1}}{\partial \sigma} \right)_{i,k} + \left[\frac{\partial}{\partial \sigma} \left(\frac{\nu_t}{D} \frac{\partial q_z^{n+1}}{\partial \sigma} \right) \right]_{i,k} \quad (14)$$

where F is an operator that includes the explicit discretization of the convective terms, the horizontal viscous terms and the Coriolis term, i and k are the cell indices, and the parameter $\theta \in [0, 1]$ (Casulli, 1999; Casulli and Zanolli, 2002).

Eventually, the governing equations can be summarized in the matrix notation:

$$\zeta_i^{n+1} + Z_{1i} \left(\frac{\partial Q_x^{n+1}}{\partial x} \right)_i + Z_{1i} \left(\frac{\partial Q_y^{n+1}}{\partial y} \right)_i = \zeta_i^n - Z_{2i} \left(\frac{\partial Q_x^n}{\partial x} \right)_i - Z_{2i} \left(\frac{\partial Q_y^n}{\partial y} \right)_i \quad (15)$$

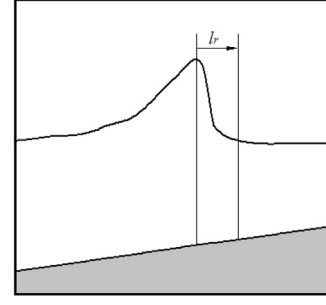


Fig. 2. Definition sketch for a breaking wave roller.

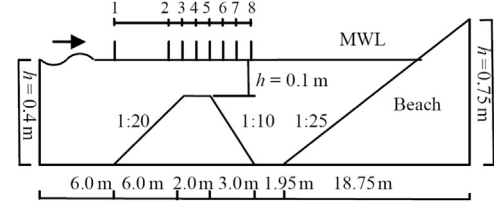


Fig. 3. Schematic of the experimental set-up in Beji and Battjes (1993).

$$A_{ix}^n Q_{xi}^{n+1} = G_{xi}^n - B_i^n \left(\frac{\partial \zeta^{n+1}}{\partial x} \right)_i - C_i^n \left(\frac{\partial p_n^{n+1}}{\partial x} \right)_i \quad (16)$$

$$A_{iy}^n Q_{yi}^{n+1} = G_{yi}^n - B_i^n \left(\frac{\partial \zeta^{n+1}}{\partial y} \right)_i - C_i^n \left(\frac{\partial p_n^{n+1}}{\partial y} \right)_i \quad (17)$$

$$A_{iz}^n Q_{zi}^{n+1} = G_{zi}^n - C_i^n \left(\frac{\partial p_n^{n+1}}{\partial \sigma} \right)_i \quad (18)$$

where

$$G_{xi}^n = [F q_{xi,1}^n \Delta \sigma_1 + \Delta t \tau_{s1} / \rho, F q_{xi,2}^n \Delta \sigma_2, \dots, F q_{xi,k}^n \Delta \sigma_k, \dots, F q_{xi,KBM}^n \Delta \sigma_{KBM}]^T,$$

$$G_{yi}^n = [F q_{yi,1}^n \Delta \sigma_1 + \Delta t \tau_{sy} / \rho, F q_{yi,2}^n \Delta \sigma_2, \dots, F q_{yi,k}^n \Delta \sigma_k, \dots, F q_{yi,KBM}^n \Delta \sigma_{KBM}]^T,$$

$$G_{zi}^n = [F q_{zi,1}^n \Delta \sigma_1, F q_{zi,2}^n \Delta \sigma_2, \dots, F q_{zi,k}^n \Delta \sigma_k, \dots, F q_{zi,KBM}^n \Delta \sigma_{KBM}]^T,$$

$$Q_{xi}^{n+1} = [q_{xi,1}^{n+1}, q_{xi,2}^{n+1}, \dots, q_{xi,k}^{n+1}, \dots, q_{xi,KBM}^{n+1}]^T,$$

$$Q_{yi}^{n+1} = [q_{yi,1}^{n+1}, q_{yi,2}^{n+1}, \dots, q_{yi,k}^{n+1}, \dots, q_{yi,KBM}^{n+1}]^T,$$

$$Q_{zi}^{n+1} = [q_{zi,1}^{n+1}, q_{zi,2}^{n+1}, \dots, q_{zi,k}^{n+1}, \dots, q_{zi,KBM}^{n+1}]^T,$$

$$B_i = [g D_i^n \Delta t \theta \Delta \sigma_1, \dots, g D_i^n \Delta t \theta \Delta \sigma_k, \dots, g D_i^n \Delta t \theta \Delta \sigma_{KBM}]^T,$$

$$C_i = [D_i^n \Delta t \Delta \sigma_1 / \rho_0, \dots, D_i^n \Delta t \Delta \sigma_k / \rho_0, \dots, D_i^n \Delta t \Delta \sigma_{KBM} / \rho_0]^T,$$

$$C'_i = [\Delta t \Delta \sigma_1 / \rho_0, \dots, \Delta t \Delta \sigma_k / \rho_0, \dots, \Delta t \Delta \sigma_{KBM} / \rho_0]^T,$$

$$Z_{1i} = [\Delta t \theta \Delta \sigma_1, \dots, \Delta t \theta \Delta \sigma_k, \dots, \Delta t \theta \Delta \sigma_{KBM}],$$

$$Z_{2i} = [\Delta t (1 - \theta) \Delta \sigma_1, \dots, \Delta t (1 - \theta) \Delta \sigma_k, \dots, \Delta t (1 - \theta) \Delta \sigma_{KBM}],$$

and A_i is a tri-diagonal matrix.

In the predictor step, the non-hydrostatic pressure is ignored, and the temporary variables q_x^* , q_y^* , q_z^* , q_σ^* are introduced. The discretized continuity and momentum equations are:

$$\zeta_i^{n+1} + Z_{1i} \left(\frac{\partial Q_x^*}{\partial x} \right)_i + Z_{1i} \left(\frac{\partial Q_y^*}{\partial y} \right)_i = \zeta_i^n - Z_{2i} \left(\frac{\partial Q_x^n}{\partial x} \right)_i - Z_{2i} \left(\frac{\partial Q_y^n}{\partial y} \right)_i \quad (19)$$

$$A_{ix}^n Q_{xi}^* = G_{xi}^n - B_i^n \left(\frac{\partial \zeta^{n+1}}{\partial x} \right)_i \quad (20)$$

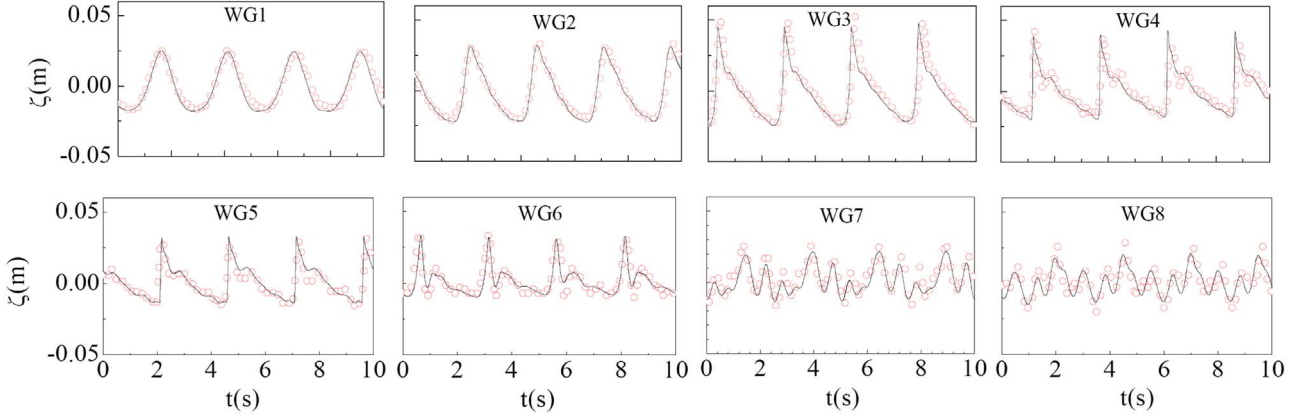


Fig. 4. Comparisons of computed (lines) and experimental (symbols) time series of free surface elevation.

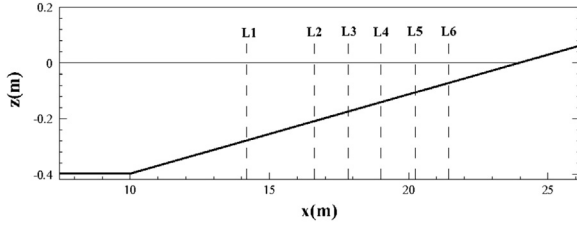


Fig. 5. Schematic of the experimental and numerical setup.

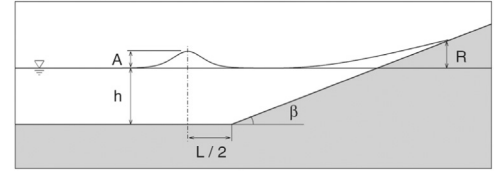


Fig. 7. Sketch of the solitary wave run-up on a plane beach (Yamazaki et al., 2009).

where $AP_{is} = \frac{Z_{li}A_{li}^{n-1}B_{li}^n y_{\eta is}}{J_{is}\Delta \xi_{is}} \cos \alpha_{is} \Delta l_{is} - \frac{Z_{li}A_{li}^{n-1}B_{li}^n x_{\eta is}}{J_{is}\Delta \xi_{is}} \sin \alpha_{is} \Delta l_{is}$, $AP_i = \Delta S_i + \sum_{s=1}^{NS} AP_{is}$. Here, NS is the total number of the cell faces around a control cell, ζ_{is}^* is the water level located at the center of the s -th neighboring cell.

The matrix system expressed in Eq. (24) is solved using the Bi-CGSTAB (Bi-Conjugate Gradients Stabilized method) method. Then, the Q_{xi}^* , Q_{yi}^* can be calculated by solving the tri-diagonal matrix system in Eqs. (20) and (21). Finally, the vertical flow variable Q_z^* is directly obtained according to Eq. (22).

In the following corrector step, Eqs. (20)–(22) are subtracted from Eqs. (16)–(18), respectively, on both sides, yielding:

$$A_{ix}^n (Q_{xi}^{n+1} - Q_{xi}^*) = -C_i^n \left(\frac{\partial p_n^{n+1}}{\partial x} \right)_i \quad (25)$$

$$A_{iy}^n (Q_{yi}^{n+1} - Q_{yi}^*) = -C_i^n \left(\frac{\partial p_n^{n+1}}{\partial y} \right)_i \quad (26)$$

$$A_{iz}^n (Q_{zi}^{n+1} - Q_{zi}^*) = -C_i^n \left(\frac{\partial p_n^{n+1}}{\partial \sigma} \right)_i \quad (27)$$

$$\zeta_i^{n+1} - Z_{li} \left\{ \frac{\partial}{\partial x} \left[A^{n-1} B^n \left(\frac{\partial \zeta^{n+1}}{\partial x} \right) \right] \right\}_i - Z_{li} \left\{ \frac{\partial}{\partial y} \left[A^{n-1} B^n \left(\frac{\partial \zeta^{n+1}}{\partial y} \right) \right] \right\}_i = BB_i \quad (23)$$

where BB_i is the combined source term. Integrating Eq. (23) over a horizontal control volume, using the Gauss's theorem and applying Eq. (8) at the cell face yield the following equation:

$$AP_{li} \zeta_i^{n+1} - \sum_{s=1}^{NS} AP_{is} \zeta_{is}^{n+1} = \langle \tilde{B}_i \rangle \quad (24)$$

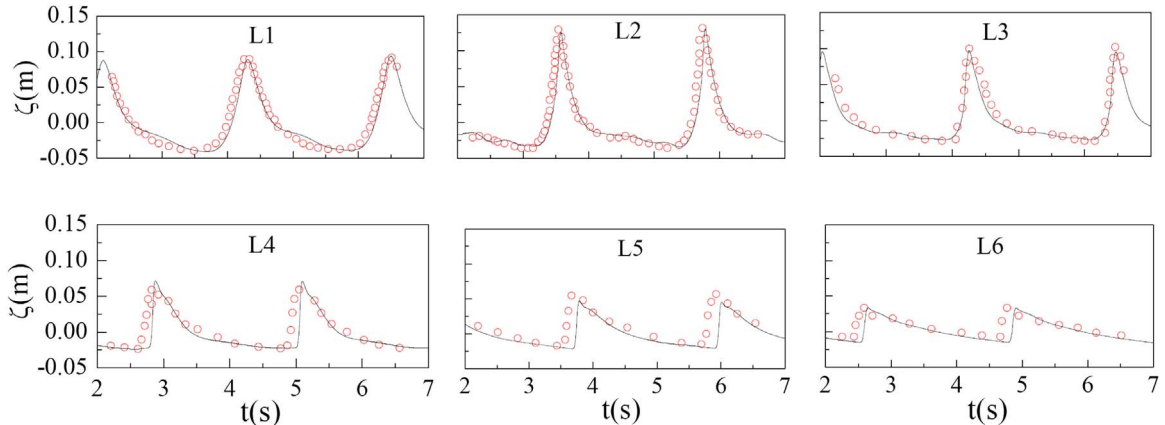


Fig. 6. Comparisons of computed (lines) and experimental (symbols) time series of free surface elevation.

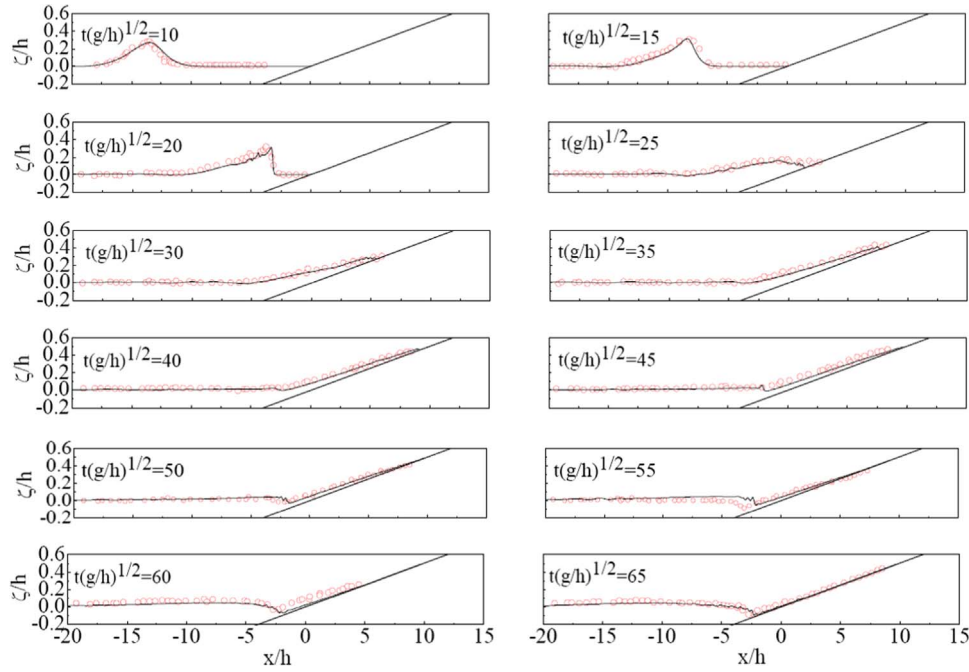


Fig. 8. Comparisons of computed (lines) and experimental (symbols) time series of free surface elevation during the solitary wave run-up on the beach.

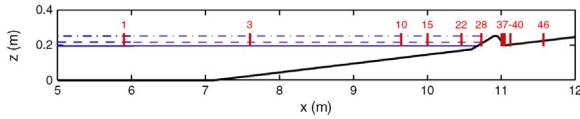


Fig. 9. Schematic of the experimental set-up (Hsiao and Lin, 2010). Horizontal lines: water levels at rest. Vertical lines: wave gauges (WG).

Table 1

Wave heights for the three experiments [28].

	h (m)	H/h
Type 1	0.20	0.35
Type 2	0.22	0.29
Type 3	0.256	0.23

The non-hydrostatic pressure enforces the corrected flow field to satisfy the continuity condition. In the σ transformed framework, the continuity Eq. (1) can be deduced to follow the following form:

$$\frac{\partial q_x}{\partial x} + \frac{\partial q_y}{\partial y} + \frac{\partial q_z}{\partial \sigma} - \frac{\partial}{\partial \sigma} \left[\frac{\partial \eta}{\partial x} (1 + \sigma) q_x + \frac{\partial \eta}{\partial y} (1 + \sigma) q_y + \frac{\partial h}{\partial x} \sigma q_x + \frac{\partial h}{\partial y} \sigma q_y \right] = 0 \quad (28)$$

A system of Poisson-type equations for the non-hydrostatic pressure p_n^{n+1} is then derived by substituting Eqs. (25), (26) and (27) into Eq. (28), which can be written as:

$$\begin{aligned} & \left[\Delta r \frac{\partial}{\partial x} \left(\frac{D}{\rho_0} \frac{\partial p_n^{n+1}}{\partial x} \right) + \Delta r \frac{\partial}{\partial y} \left(\frac{D}{\rho_0} \frac{\partial p_n^{n+1}}{\partial y} \right) + \Delta r \frac{\partial}{\partial \sigma} \left(\frac{1}{\rho_0} \frac{\partial p_n^{n+1}}{\partial \sigma} \right) \right]_{i,k} \\ &= \left(\frac{\partial q_x^*}{\partial x} \right)_{i,k} + \left(\frac{\partial q_y^*}{\partial y} \right)_{i,k} + \left(\frac{\partial q_z^*}{\partial \sigma} \right)_{i,k} \\ & - \frac{\partial}{\partial \sigma} \left[\frac{\partial \eta^*}{\partial x} (1 + \sigma) q_x^* + \frac{\partial \eta^*}{\partial y} (1 + \sigma) q_y^* + \frac{\partial h}{\partial x} \sigma q_x^* + \frac{\partial h}{\partial y} \sigma q_y^* \right]_{i,k} \end{aligned} \quad (29)$$

where the cross-derivative terms of p_n^{n+1} have been neglected. The final discretized matrix system concerning Eq. (29) can be summarized to

be:

$$AP_{i,k} p_{ni,k}^{n+1} - AP_{i,k}^T p_{ni,k-1}^{n+1} - AP_{i,k}^B p_{ni,k+1}^{n+1} - \sum_{s=1}^{NS} AP_{i,k}^s p_{ni,s}^{n+1} = \widetilde{BP}_{i,k} \quad (30)$$

where

$$AP_{i,k}^s = \Delta t \Delta \sigma_k \left\langle \frac{D \Delta l_{is}}{\rho_0 J_{is} \Delta \xi_{is}} (\cos \alpha_{is} y_\eta - \sin \alpha_{is} x_\eta) \right\rangle^f, \quad AP_{i,k}^T = \frac{\Delta t \Delta s_i}{D \rho_0 \Delta \sigma_{k-1/2}},$$

$$AP_{i,k}^B = \frac{\Delta t \Delta s_i}{D \rho_0 \Delta \sigma_{k+1/2}}, \quad AP_{i,k} = \sum_{s=1}^{NS} AP_{i,k}^s + AP_{i,k}^T + AP_{i,k}^B,$$

$p_{ni,s}^{n+1}$ is the pressure in the s -th neighboring cell ni , and $(\cos \alpha_{is}, \sin \alpha_{is})$ are the x - and y - components of the unit vector of the face i .

At the solid wall and the bottom bed, a zero normal gradient of the pressure p_n is imposed. At the free surface, the pressure is specified to be zero. After the Poisson-type equation is solved, the updated flow velocities are calculated.

2.4. Treatment of wave breaking

Prior to wave breaking, the non-hydrostatic model can give a very accurate description of the wave transformation. However, the depth-averaged approaches cannot reproduce wave overturning and the detailed processes during wave breaking. Hence, approximate representations of the physical process are required. The breaking wave is analogy to the hydraulic jump, and the wave front can be represented as a shock, which allows mechanical energy to dissipate. The non-hydrostatic model is locally switched to the hydrostatic model to handle wave breaking, noting the ability of NSW in simulating shock waves. The NSW mode is only switched in the local breaking wave front, which is implemented by means of locally skipping the corrector step when the wave is ready to break. This similar idea of suppressing the wave dispersive effect has been also adopted by BT models (Tissier et al., 2012).

2.4.1. Breaking criteria

The criteria of the initiation of wave breaking have been discussed in the literature (Zelt, 1991; Kennedy et al., 2000; Tissier et al., 2012). The maximum wave slope $|d\zeta/dx|$ over the wave front is considered as

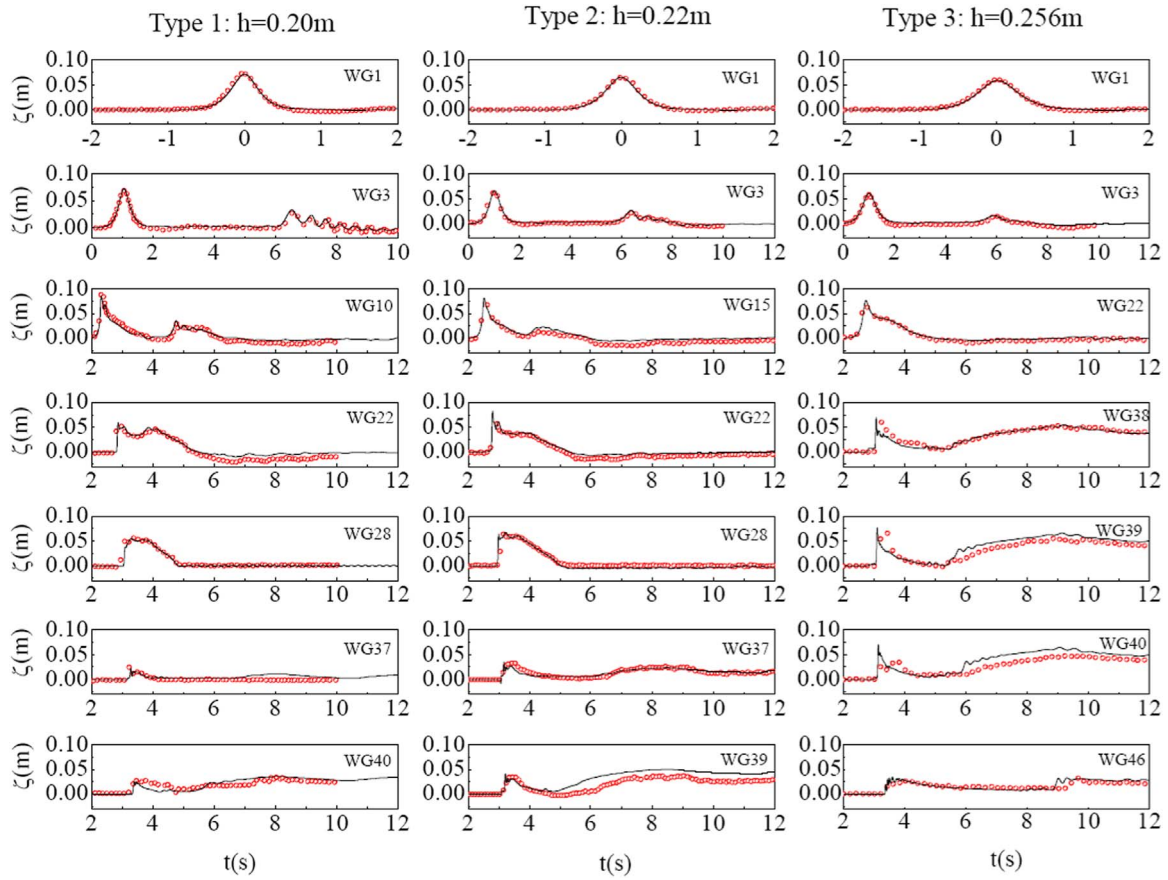


Fig. 10. Comparison of measured (symbols) and calculated (lines) time series of water elevation.

an indicator for each breaker. In the frame moving with each individual wave, the threshold for the wave breaking to start and stop are summarized as follows. Wave breaking starts if $|d\zeta/dX| \geq \tan \Phi_b$, whereas wave breaking stops if $|d\zeta/dX| \leq \tan \Phi_f$, with Φ_b = limiting angle for the inception of wave breaking and Φ_f = limiting angle for the termination of wave breaking.

2.4.2. Suppression of wave dispersion

In the wave roller model, wave breaking takes place over a region at the local wave front with a horizontal length l_r , which is labeled in Fig. 2 as the distance from the wave crest to the front edge of the wave. When a wave is about to break, the non-hydrostatic pressure term is then excluded in the computation over the spatial extent l_r at the wave front.

Numerical experiments have shown that the prediction of the wave breakings is strongly dependent on l_r (Cienfuegos et al., 2010; Tissier et al., 2012). In the present study, the l_r value is $0.82h$ for a fully-developed breaking wave, with h being the still local water depth. This value is then subjected to a lower bound of twice the local grid size. However, adopting a constant length l_r over time often induces over-prediction of wave breaking effects, because the wave breaking length should in reality gradually increase from zero to l_r over time. Hence, a gradually increase of the roller length is more reasonable. In the following case studies, a linear increase of the roller length to the full length l_r is adopted during a wave period.

The non-hydrostatic pressure term is instantaneously removed once the wave begins to break, which may induce a non-smoothing numerical result. The numerical instability induced by such a splitting algorithm shall be avoided. A Gaussian filter is locally applied over the wave breaking zone in the present numerical model to smooth out the numerical fluctuations.

3. Results and analysis

In order to evaluate the ability of the present model in simulating the wave dynamics in the surf zone, we performed several numerical test cases. They involved the transformation of regular wave trains over a bar, shoaling and breaking of regular waves on a sloping beach, solitary wave propagation over a sloping beach, wave overtopping and solitary wave run-up on a conical island. Detailed experimental data are available for validating the numerical schemes and the wave-breaking treatment. At last, a hypothetical tsunami-type wave overtopping and inundation case study was used to demonstrate the numerical model's capability in simulating the wave dynamics over complex topography.

3.1. Periodic waves breaking over a bar

Beji and Battjes (1993) conducted a series of flume experiments concerning the propagation of regular waves over a submerged trapezoidal bar. The long wave plunging case ($f = 0.4$ Hz) as described in a series of experiments was simulated with the present model. The bathymetry specified in the numerical simulation is presented in Fig. 3. Eight wave gauges (WG) were deployed, numbered from 1 to 8. The time series of recorded surface elevations are used to validate the present numerical model, with an emphasis on the wave evolution over the bar. The computational grid sizes are $\Delta x = \Delta y = 2\text{ cm}$ in horizontal plane. In the vertical direction, the first grid point to the bottom is maintained at about $3.0z^+$, with a stretching ratio of about 1.15 between adjacent grid cells resulting in a total 28 vertical layers. Such a configuration of the vertical layers is adopted in all the subsequent cases. The time step is $\Delta t = 0.001\text{ s}$.

Fig. 4 presents the comparison of the computed and measured water elevations at the locations of the eight wave gauges. The wave

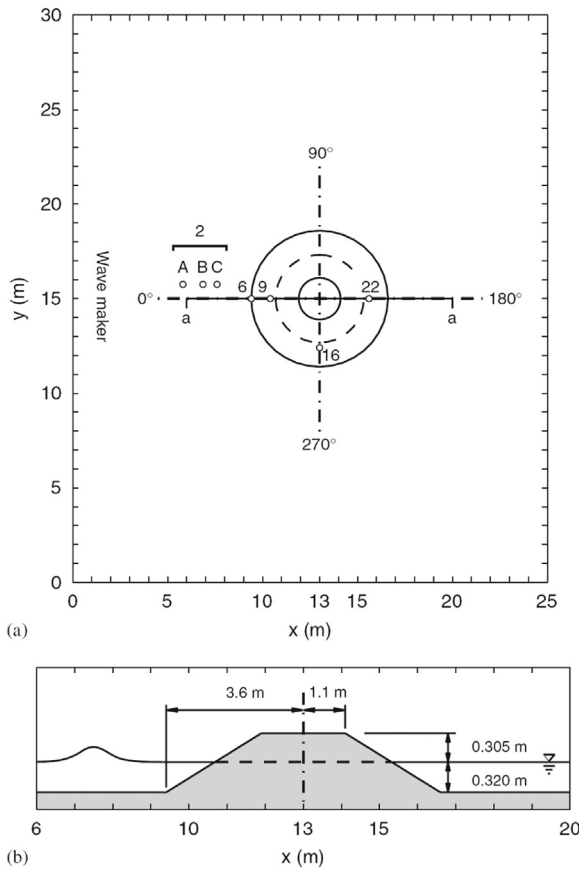


Fig. 11. Schematic of the conical island experiment (Yamazaki et al., 2009). (a) plane view, with gauge locations. (b) side view.

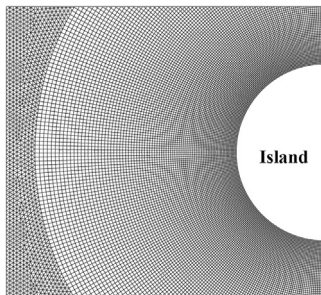


Fig. 12. Horizontal local meshes around the island.

propagating and shoaling on the front face of the bar is accurately simulated (WG1 and WG2). The incident wave front becomes steeper and steeper when approaching the bar crest without breaking in the present non-hydrostatic mode. The wave begins to break at site 3, and stops the breaking at site 5. In the simulation, the hydrostatic mode is switched over the wave front during the wave propagating over the bar crest. Further downstream, the wave-breaking stops, but waves with higher frequencies emerge. After waves stop breaking, the non-hydrostatic mode is again activated. The comparison presented in Fig. 4 reveals a good overall agreement with the experimental data.

3.2. Breaking of regular waves over a sloping beach

The Cox (1995)'s regular wave experiment was used to validate the simulations of the regular waves shoaling and breaking in the surf zone. The still water depth in front of the beach is $h = 0.4\text{m}$, and the planar beach is of a slope 1:35. The incident cnoidal waves of relative amplitude $H/h = 0.29$ and period $T = 2.2\text{s}$ are specified in the present

study case. The computation uses $\Delta x = \Delta y = 2\text{cm}$ in horizontal plane, and the time step is $\Delta t = 0.001\text{s}$. Time series of free surface elevations are available at six locations labeled from L1 to L6 in Fig. 5, corresponding to wave gauges (WG) located along the beach. In the experiment, the waves were observed to undergo slightly breaking at L2. L1 and L2 are outside the surf zone, whereas L3 to L6 are inside the surf zone.

Fig. 6 compares the experimental and numerical time series of the free surface elevations. Overall, the calculated results coincide well with the measured ones in both the shoaling and surf zones. The fully broken wave at L4 is slightly overestimated in height by the model, with a slightly overestimated steepness of the wave front. However, the wave heights are underestimated at L5 and L6. Apart from the discrepancies of the wave heights, a small phase lag at L5 and L6 is also observed, which is a consequence of the underestimation of the wave height in those positions. The smaller wave heights result in a lower wave speed and thus the delayed arrival of the wave front. In the surf zone, the waves continually break on the shore, and the breaking criteria varies with time (Fredsoe and Deigaard, 1992). A constant breaking criterion adopted in the present model is efficient and practical for wave breaking simulation over complex geometry, but may give rise to small errors.

3.3. Solitary wave run-up over a sloping beach

The experiment carried out by Synolakis (1987) concerning an incident solitary wave was used to assess the ability of the present model in simulating solitary wave breaking and run-up. The relative amplitude is $A/h = 0.28$, where $h = 0.3\text{m}$ is the still water depth in front of the beach. A is the initial wave height, and the beach has a slope of 1:19.85. The experimental and numerical setup is shown in Fig. 7. The initial water surface level and velocity are given by the theoretical solution of the KDV equation. The initial distance $L/2$ from the wave crest to the beach toe is calculated by the formula cited in the reference (Titov and Synolakis, 1995). The computation uses $\Delta x = \Delta y = 2\text{cm}$ on horizontal plane, and $\Delta t = 0.001\text{s}$.

The instantaneous wave profiles were recorded during the run-up and run-down of the solitary wave, from which the movement of the shoreline can be clearly observed. The comparisons of the water elevation snapshots are presented in Fig. 8, which reveals a good overall agreement with experimental data. The predicted wave transformation in shoaling is clearly revealed in Fig. 8 at moment $t(g/h)^{1/2} = 10$ and $t(g/h)^{1/2} = 15$. The wave starts to break at non-dimensional time $t(g/h)^{1/2} = 20$. The predicted wave front is slightly steeper than the measured one. It is noticeable that there are a few small undulations on the lee side of the wave, which is possibly due to the numerical instability induced by the switching from the non-hydrostatic mode to the hydrostatic mode during the wave-breaking simulation. However, it is noted that these undulations are also recorded in the experiments, corresponding to the violent nature of the wave breaking. During the wave run-up, i.e. $t(g/h)^{1/2} = 25\sim 40$, a small lag of the shoreline motion is predicted. A faster predicted motion of the shoreline during wave run-down, i.e. $t(g/h)^{1/2} = 45\sim 65$ is observed from the comparisons. The run-down wave trough movement is predicted to be slightly slower than the measured value at $t(g/h)^{1/2} = 50\sim 65$.

3.4. Solitary waves overtopping a seawall

A series of transformations of solitary waves overtopping a seawall were used to investigate the ability of the present model in complex situations. The experiments were carried out by Hisao and Lin (2010) in a 22 m long wave flume. During the experiments, three solitary waves were generated with different still water depths, as seen in Fig. 9. Table 1 summarizes the incident wave parameters. The computation uses $\Delta x = \Delta y = 2\text{cm}$ in horizontal plane, and $\Delta t = 0.001\text{s}$. Comparisons

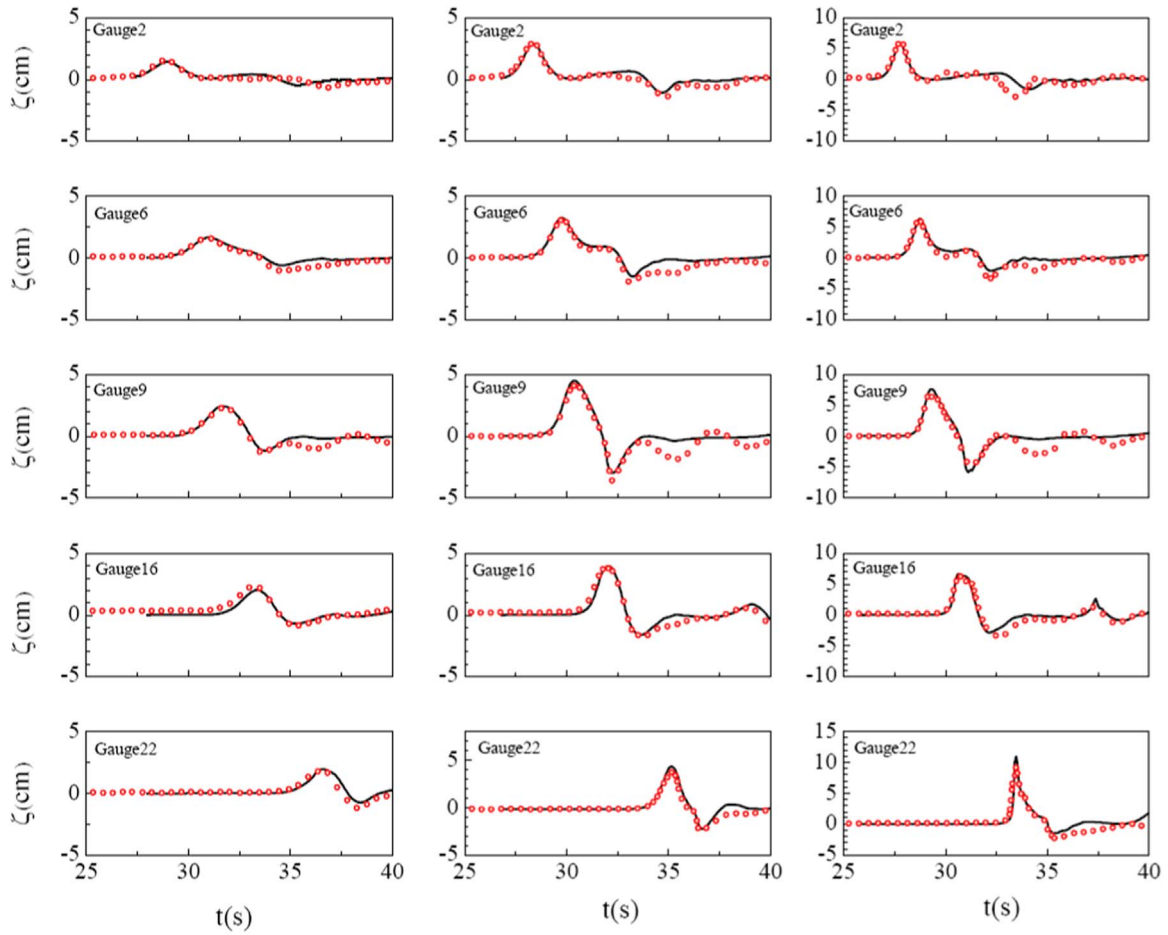


Fig. 13. Comparison of measured (symbols) and calculated (lines) time series of water elevation.

between the measured and calculated time series of the water elevations at seven gauges are presented in Fig. 10. The left column is the comparison between measured and numerical time series of free surface elevations at the gauges in the first test case. The middle and the right columns are for the comparisons in the second and third test cases, respectively.

In the first test case, the incident wave was breaking on the sloping beach before reaching the seawall. Not only the incident wave but also the reflected wave are accurately predicted by the present model, as seen in the water elevation variations at WG3, WG10 and WG22. There is slight discrepancy of the elevation during wave run-down on the lee side of the seawall at WG40, which can be attributed to the strong turbulence and air entrainment generated as the wave collapses behind the seawall. In the second test case, the incident solitary wave breaks on the seawall. The wave transformation on the beach in front of the seawall and the wave overtopping are accurately predicted by the numerical model, except some noticeable disagreement behind the seawall shown at WG39. In the third test case, the incident solitary wave was weakly breaking in front of the seawall, and significant wave overtopping occurs over the seawall. The wave collapsing behind the seawall is very complex with possible air entrainment, so the validation shows relatively low accuracy in the numerical prediction of the flows, as seen in WG38–WG46. Despite the discrepancy between the measured and predicted time series of the free surface, it is encouraging to note that the predicted water depths behind the seawall slowly reach the measured values with increasing time, which suggests an accurate prediction of the amount of the overtopped water. The performance of the present model is similar to that of a BT model (Tissier et al., 2012). Overall, a very good agreement of the wave shoaling and breaking in

front of the seawall is obtained, and the volume of overtopped water is reasonably predicted by the present model.

3.5. Solitary wave run-up on a conical island

In order to examine the present model in handling multi-directional wave propagation and breaking, a large-scale laboratory experiment of solitary wave wrapping a conical island was used as a three-dimensional test case. The experimental data from Briggs et al. (1995) have been widely used to validate wave run-up models. The schematic of the experimental setup is shown in Fig. 11, as given in Yamazaki et al. (2009). In the simulation, the incident wave is generated by means of initially specifying the solitary wave field inside the domain instead of moving a paddle wave maker on one side of the basin. The present study only considers the water depth $h = 0.32\text{m}$ to validate the model. Three initial wave heights of $A/h = 0.045, 0.096$ and 0.181 were specified in the numerical study cases here. According to Fig. 11, Gauges 2 and 6 were located in front of the island and Gauges 9, 16, and 22 were placed just outside the still waterline around the island. The records of the free surface elevations at these gauges provide sufficient details of the wave transformation around the island. The computation uses unstructured grids with a finest horizontal grid size $\Delta l = 2\text{cm}$ near the island and a coarser grid size $\Delta l = 10\text{cm}$ near horizontal boundaries of the domain (Fig. 12). The time step is specified to be $\Delta t = 0.001\text{s}$.

There was no wave breaking at $A/h = 0.045$, and the free-surface elevation is predicted rather smooth, as seen in the left column of Fig. 13. There is a good agreement between the calculated incident solitary wave profile and the measured one, but the high-frequency

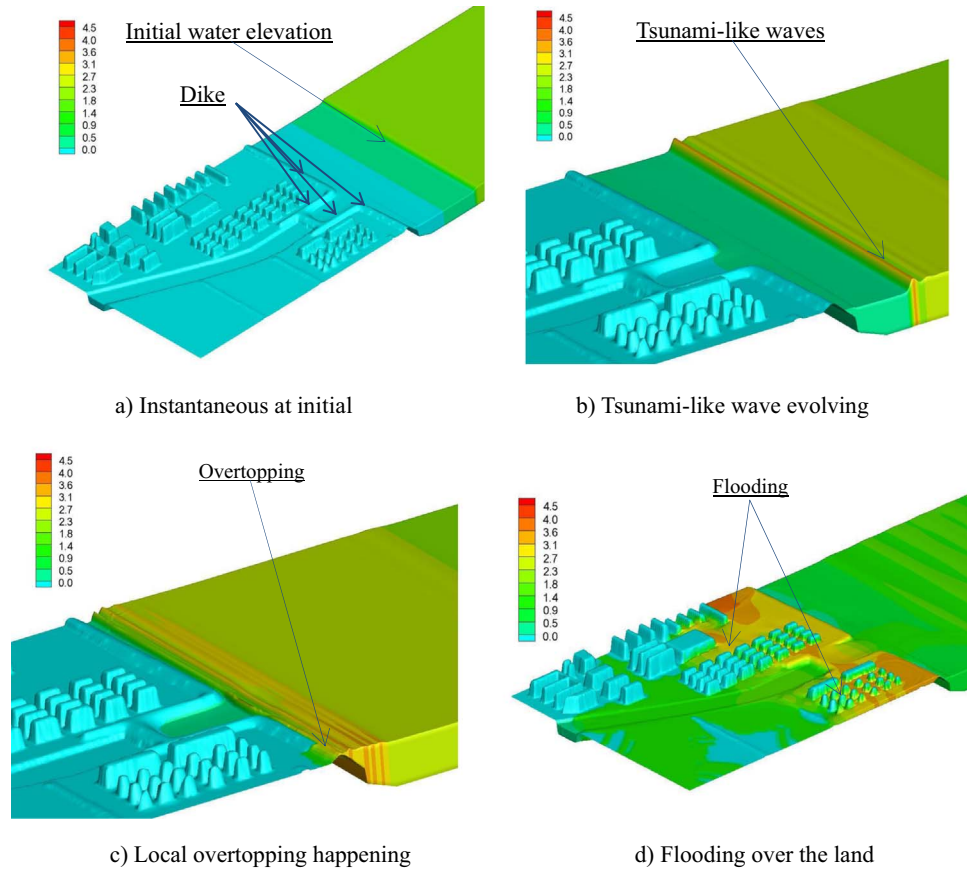


Fig. 14. Predicted wave transformation and water depth distribution in a coastal region (the color legend for water elevations in meters). a) Instantaneous at initial b) Tsunami-like wave evolving c) Local overtopping happening d) Flooding over the land.

reflected dispersive waves are under-predicted at Gauge 9. Similar discrepancies between calculated and measured results at Gauge 9 for $A/h = 0.045$ and 0.181 are also observed in the present study. Gauge 9 was located near the waterline, and the local water depth is relatively small, which makes it easy to introduce experimental and computational errors. Overall, the incident wave crest and the subsequent wave rundown are predicted very well in comparison to the measured results for the three incident solitary waves. For $A/h = 0.096$, the wave was locally breaking, and for $A/h = 0.181$, the wave breaking occurred generally around the island. Fig. 13 reveals a good prediction of the steep breaking wave's transformation, especially at Gauge 22 for $A/h = 0.181$. The large wave height leads to a larger wave celerity. For $A/h = 0.045$, the wrapped waves arrived at Gauge 16 at time 39.12 s, whereas for $A/h = 0.181$ the recorded time was reduced to 37.34 s. The numerical prediction of the wave wrapping the island coincides well with the measurements.

3.6. Tsunami-like wave inundation of a small coastal town

The present efficient model is useful for predicting the overtopping and inundation induced by storm surges and tsunami-like large waves. In the present study, a coastal region was used to demonstrate the ability of the model in simulating the flooding over real terrains. The area is a 2 km by 2 km square protected by a long dike with a height of 1.5 m above the still water level. The outer flat seabed is specified to be -10 m in elevation, i.e. 10 m below the still water level. The finest grid size of 2 m is used to describe the buildings, and the coarser grid size is used in seaward region and the inland region without building presence. The initial seaside water level and velocity fields are defined by the following Eq. (31) to generate an initial tsunami-like wave.

$$\begin{cases} h(x, 0) = \frac{1}{2}(h_2 - h_1)(1 - \tan(x/l)) + h_1 \\ u(x, 0) = \frac{1}{2}(u_2 - u_1)(1 - \tan(x/l)) + u_1 \end{cases} \quad (31)$$

where h_1 and h_2 are the water depths in front and behind the wave, respectively, u_1 and u_2 are the corresponding depth-averaged velocities. In the present simulation, $u_1 = 0$, $u_2 = 10.8$ m/s, $h_1 = 10$ m, $h_2 = 12$ m, and a transitional length $l = 10$ m are specified. The Froude number Fr defined by (Tissier et al., 2012) is about 1.14 , and the initial tsunami wave evolves into an undular bore without breaking until reaching the front toe of the sea dike. The Fig. 14(b) reveals the undular bore waves traveling shoreward, which is realistically predicted by the present model. The wave overtopping occurs locally over the breakwater as shown in Fig. 14(c). Fig. 14(d) shows that the flooding appears in most of the coastal area. Although this study is only hypothetical, the evolution of the tsunami wave and the flooding process are reasonably predicted.

4. Conclusions

This paper describes a 3D non-hydrostatic flow model for coastal wave propagation, transformation, breaking, run-up and inundation. The formulation decomposes the full pressure into the hydrostatic and non-hydrostatic components. The hydrostatic flow model is equivalent to the nonlinear shallow water equations model. The wave breaking phenomenon is simply handled by locally switching the model from the non-hydrostatic mode to the hydrostatic mode in order to suppress the spurious water surface oscillations. No additional parameterization is required to simulate wave breaking. The present model satisfactorily reproduces the results obtained in several well-known experiments. These experiments have been widely used to validate numerical models in predicting coastal processes. The present numerical scheme is

verified to be highly efficient and accurate in the numerical simulations.

The commonly-used benchmarks with simple topography have reasonably validated the non-hydrostatic model, but the applicability of the present model in simulating wave progressing over complex topography has not been quantitatively validated. In the next stage of our research, this model will be applied to simulate the large-scale real-world coastal processes, with field measured data available for detailed assessment of the model's ability.

Acknowledgments

This work was supported by the National Natural Science Foundation (No. 51479111 and No. 11572196) and the National Basic Research Program (973 program) of China (No. 2014CB046200).

References

- Beji, S., Battjes, J.A., 1993. Experimental investigation of wave propagation over a bar. *Coast. Eng.* 19 (1–2), 151–162.
- Bonneton, P., Chazel, F., Lannes, D., Marche, F., Tissier, M., 2011b. A splitting approach for the fully nonlinear and weakly dispersive Green-Naghdi model. *J. Comput. Phys.* 230, 1479–1498.
- Borthwick, A.G., Barber, R.W., 1992. River and reservoir flow modeling using the transformed shallow water equations. *Int. J. Numer. Methods Fluids* 14, 1193–1217.
- Briggs, M.J., Synolakis, C.E., Harkins, G.S., Green, D.R., 1995. Laboratory experiments of tsunami runup on a circular island. *Pure Appl. Geophys.* 144 (3/4), 569–593.
- Casulli, V., 1999. A semi-implicit finite difference method for non-hydrostatic, free-surface flows. *Int. J. Numer. Methods Fluids* 30, 425–440.
- Casulli, V., Cattani, E., 1994. Stability, accuracy and efficiency of a semi-implicit method for three-dimensional shallow water flow. *Comput. Math. Appl.* 7 (4), 99–112.
- Casulli, V., Zanolli, P., 2002. Semi-implicit numerical modeling of nonhydrostatic free-surface flows for environmental problems. *Math. Comput. Model.* 36, 1131–1149.
- Chen, R., Shao, S., Liu, X., Zhou, X., 2015. Applications of shallow. *Water SPH Model Mt. Rivers J. Appl. Fluid Mech.* 8 (4), 863–870.
- Chen, X.J., 2003. A fully hydrodynamic model for three-dimensional, free-surface flows. *Int. J. Numer. Methods Fluids* 42, 929–952.
- Cienfuegos, R., Barthélemy, E., Bonneton, P., 2010. Wave-breaking model for Boussinesq-type equations including roller effects in the mass conservation equation. *J. Waterw., Port., Coast. Ocean Eng.* 136 (1), 10–26.
- Cox, D.T., 1995. Experimental and numerical modeling of surf zone hydrodynamics. (Ph. D. thesis). University of Delaware, Newark, Del.
- Darwish, M.S., Moukalled, F., 2003. TVD schemes for unstructured grids. *Int. J. Heat. Mass Transf.* 46, 599–611.
- Fredsoe, J., Deigaard, R., 1992. *Mechanics of coastal sediment transport*. World Scientific publishing Co. Pte. Ltd..
- Fringer, O.B., Gerritsen, M., Street, R.L., 2006. An unstructured-grid, finite-volume, nonhydrostatic, parallel coastal ocean simulator. *Ocean Model.* 14, 139–173.
- Hsiao, S.C., Lin, T.C., 2010. Tsunami-like solitary waves impinging and overtopping an impermeable seawall: experiment and RANS modeling. *Coast. Eng.* 57, 1–18.
- Jankowski, J.A., 1999. A non-hydrostatic model for free surface flows (Ph.D. Dissertation). University of Hannover, Germany.
- Karambas, T., Koutitas, C., 1992. A breaking wave propagation model based on the Boussinesq equations. *Coast. Eng.* 18, 1–19.
- Kennedy, A., Chen, Q., Kirby, J., Dalrymple, R., 2000. Boussinesq modeling of wave transformation, breaking and runup. I: 1D. *J. Waterw., Port., Coast., Ocean Eng.* 126 (1), 39–48.
- Kocyyigit, M.B., Falconer, R.A., Lin, B., 2002. Three-dimensional numerical modeling of free surface flows with non-hydrostatic pressure. *Int. J. Numer. Methods Fluids* 40, 1145–1162.
- Li, B., Fleming, C.A., 2001. Three-dimensional model of Navier-Stokes equations for water waves. *J. Waterw., Port., Coast. Ocean Eng.* 127 (1), 16–25.
- Liang, D., 2010. Evaluating shallow water assumptions in dam-break flows. *Proc. Inst. Civil. Eng. – Water Manag.* 163 (5), 227–237.
- Liang, D., Falconer, R.A., Lin, B., 2006. Improved numerical modelling of estuarine flows. *Proc. Inst. Civil. Eng. – Marit. Eng.* 159 (1), 25–35.
- Ma, G.F., Shi, F.Y., Kirby, J.T., 2012. Shock-capturing non-hydrostatic model for fully dispersive surface wave processes. *Ocean Model.* 43–44, 22–35.
- Pu, J.H., Shao, S., Huang, Y., Hussain, K., 2013. Evaluations of SWEs and SPH numerical modeling techniques for dam break flows. *Eng. Appl. Comput. Fluid Mech.* 7 (4), 544–563.
- Schäffer, H., Madsen, P., Deigaard, R., 1993. A Boussinesq model for waves breaking in shallow water. *Coast. Eng.* 20, 185–202.
- Spalart, P.R., 2000. Strategies for turbulence modelling and simulations. *Int. J. Heat. Fluid Flow.* 21, 252–263.
- Synolakis, C.E., 1987. The runup of solitary waves. *J. Fluid Mech.* 185, 523–545.
- Tissier, M., Bonneton, P., Marche, F., Chazel, F., Lannes, D., 2012. A new approach to handle wave breaking in fully non-linear Boussinesq models. *Coast. Eng.* 67, 54–66.
- Titov, V.V., Synolakis, C.E., 1995. Modeling of breaking and nonbreaking long-wave evolution and run-up using VTCS-2. *J. Waterw., Port., Coast., Ocean Eng.* 121 (6), 308–316.
- Wei, Z.P., Jia, Y.F., 2014. Non-hydrostatic finite element model for coastal wave processes. *Coast. Eng.* 92, 31–47.
- Yamazaki, Y., Kowalik, Z., Cheung, K.F., 2009. Depth-integrated, non-hydrostatic model for wave breaking and run-up. *Int. J. Numer. Meth. Fluids* 2009, 473–497.
- Zelt, J., 1991. The run-up of non-breaking and breaking solitary waves. *Coast. Eng.* 15, 205–246.
- Zhang, J.X., Liu, H., 2009. Wave run-up on a vertical seawall protected by an offshore submerged barrier. *China Ocean Eng.* 23 (3), 553–564.
- Zhang, J.X., Sukhodolov, A.N., Liu, H., 2014. Fully hydrodynamic versus hydrostatic modeling for shallow environmental flows. *J. Hydrodyn.* 26 (4), 840–847.